DAMPING OPTIMIZATION OF VISCOELASTIC CANTILEVER BEAMS AND PLATES UNDER FREE VIBRATION

A Joubert, G Allaire, S Amstutz, J Diani

A Joubert, G Allaire, S Amstutz, J Diani. DAMPING OPTIMIZATION OF VISCOELASTIC CANTILEVER BEAMS AND PLATES UNDER FREE VIBRATION. Computers & Structures, 2022. hal-03663567

HAL Id: hal-03663567

https://hal.science/hal-03663567

Submitted on 10 May 2022

DAMPING OPTIMIZATION OF VISCOELASTIC CANTILEVER BEAMS AND PLATES UNDER FREE VIBRATION

A. JOUBERT[1], G. ALLAIRE[2], S. AMSTUTZ[3], AND J. DIANI[4]

Abstract. The goal of this work is to significantly enhance the damping of linear viscoelastic structures under free vibration by relying on optimal design. Homogeneous cantilever slender beams and plates satisfying, respectively, the Euler-Bernoulli and Kirchhoff-Love assumptions are considered. A sizing optimization of the beam or plate thickness is proposed, as well as a coupled optimization of the thickness and geometry of the plate applying Hadamard's boundary variation method. The isotropic linear viscoelastic material is modeled by a classical generalized Maxwell model, well suited for polymers. Gradients of the objective functions are computed by an adjoint approach. Optimization is performed by a projected gradient algorithm and the mechanical models are evaluated by the finite element method. Numerical tests indicate that the optimal designs, as well as their damping properties, strongly depend on the material parameters.

[1] Laboratoire de Mécanique des Solides LMS, CNRS UMR 7649, École Polytechnique, Institut Polytechnique de Paris, Route de Saclay, 91128 Palaiseau, France.
Email: antoni.joubert@polytechnique.edu
[2] Centre de Mathématiques Appliquées CMAP, CNRS UMR 7641, École Polytechnique, Institut Polytechnique de Paris, Route de Saclay, 91128 Palaiseau, France.
Email: gregoire.allaire@polytechnique.edu
[3] Centre de Mathématiques Appliquées CMAP, CNRS UMR 7641, École Polytechnique, Institut Polytechnique de Paris, Route de Saclay, 91128 Palaiseau, France.
Email: samuel.amstutz@polytechnique.edu
[4] Laboratoire de Mécanique des Solides LMS, CNRS UMR 7649, École Polytechnique, Institut Polytechnique de Paris, Route de Saclay, 91128 Palaiseau, France.
Email: julie.diani@polytechnique.edu

Key words. Free vibration, Damping, Linear viscoelasticity, Eigenvalue optimization, Optimal design.

Acknowledgements. This action benefited from the support of the Chair "Modelling advanced polymers for innovative material solutions" led by Ecole polytechnique (l'X) and the Fondation de l'Ecole polytechnique and sponsored by Arkema.

1. Introduction

Viscoelastic damping materials, such as elastomers or polymers within their glass transition, are widely used to absorb vibrations of structures. The polymer linear viscoelastic properties exhibiting several relaxation times, well reproduced by rheological models such as the generalized Maxwell model, confer them a large range of applications [35]. The current paper focuses on finding the optimal design of viscoelastic cantilever beams and plates to maximize their damping capacities.

The optimal material distribution is reached using sizing and shape optimization methods. While the former allows the optimization of one or more design variables such as the thickness, the latter seeks for the optimal shape of the domain which becomes the design variable. These methods are well known and very efficient within the elastic framework, for various objective functions such as compliance, maximal displacements, von Mises stress and so on (see textbooks [7, 1, 2]). Optimal design of elastic structures for frequency response is also a classical topic [29, 3]. Even if the extension of these methods to viscoelastic materials is rather recent, some contributions have to be mentioned. In the scope of the design sensitivity analysis for transient response of damped systems, Yun and Youn [36] used the adjoint method and, more recently, Ding et al. [15] used model order reduction techniques. Various numerical techniques are employed to find the optimal distribution of viscoelastic material. Among these, density-based methods are commonly used to perform topology optimization of microstructures, multilayered materials or layer damping treatments. Andreassen and Jensen [5] investigated the topology optimization of periodic microstructures in order to maximize the attenuation of propagating waves. Elsabbagh and Baz [16] conducted the topology optimization of unconstrained layer damping (UCLD) treatments, optimizing the distribution of the viscoelastic treatment. Zhang and Khandelwal [38] proposed the topology optimization of multimaterial dissipative systems at finite strains. More specifically, the popular solid isotropic material with penalization (SIMP) method is considered in a number of works. Kang et al. [27] carried out the topology optimization of damping layers in shell structures under harmonic excitations by optimizing the distribution of damping material. Chen and Liu [12] conducted the microstructural topology optimization of viscoelastic structures, in view of maximizing the modal loss factor. James and Waisman [25, 26] proposed the topology optimization for minimum mass of viscoelastic structures subjected to dynamic loads using a time-dependent adjoint method. Yun and Youn [37] performed the topology optimization of damping layers attached to shell structures. More recently, Fang et al. [17] proposed the topology optimization of plates with constrained layer damping (CLD) treatments to maximize the modal loss factor. Other methods for structural topology optimization have been applied to viscoelastic materials, such as the Bidirectional Evolutionary Structural Optimization (BESO) method or the evolutionary structural optimization (ESO) method. Liu et al. [28] applied the BESO method to maximize the modal loss factor of composite materials. Fang and Zheng [18] applied the ESO method to the minimization of the resonant response of plates with CLD treatment. Boundary variation methods, such as the level-set method, have also been applied to layer damping treatments. Ansari et al. [6] used the level-set approach to find the optimal shape and location of CLD patches onto the surface of plate structures. In a recent paper from Delgado and Hamdaoui [13], the level-set method is employed to perform the structural optimization of multilayered and homogeneous viscoelastic structures.

The goal of the present paper is to go further on the optimization of homogeneous viscoelastic structures using Hadamard's boundary variation method. We optimize the thickness profile of a cantilever beam, and we simultaneously optimize the thickness profile and the shape of a cantilever plate, in order to maximize the damping of these structures under free vibration. The main novelty here is the representation of the viscoelastic properties of polymers by a generalized Maxwell model taking into account the frequency dependence of Poisson's ratio. This more general model introduces some nonlinearity in the problem. We also study the impact of viscoelastic parameters on the optimization, such as relaxation times but now also Poisson's ratios, without neglecting their frequency dependence. Coupled optimization techniques are also adapted to perform the optimization of homogeneous viscoelastic plates. Coupled optimization of two different sets of design parameters, such as thickness and geometry here, is a classical issue. Let us mention some other examples like geometry and topology optimization (for example, coupling the level-set method with the topological gradient), shape and infill optimization, shape and anisotropy (for example, for fiber reinforced composites). Additionally, this paper includes a comparison of possible cost functions related to damping optimization and raises issues concerning the modal loss factor in particular.

The main results of this work are, on the theoretical side, the rigorous derivation of sizing and shape sensitivities by the adjoint approach, which is new, to the best of our knowledge, for a generalized Maxwell model with frequency-dependent Poisson's ratio, and, on the numerical side, the optimization of cantilever beams and plates as well as a sensitivity analysis of the viscoelastic parameters. Our numerical examples show that the optimal designs are very sensitive to the material parameters, with a possible inversion of the thickness profile when the relaxation time is varying.

This paper is organized as follows. Section 2 presents the bending vibration problem of a cantilever beam. The sizing optimization equations are detailed as well as the sensitivity analysis of the objective function with respect to the design variables. The optimized profiles of the beam have been estimated according to the material parameters using finite element methods. Section 3 focuses on the bending vibration of a cantilever plate and its coupled optimization. The derivatives of the cost function and the numerical methods are detailed. The sizing and shape optimization problems are extensively discussed before studying the impact of the material properties. Finally, the opposite problem aiming at limiting the vibration damping of the cantilever plate, which may draw some interest in sport applications, is examined.

2. Optimization of the free vibration damping of a linear viscoelastic beam

2.1. **Free vibration problem.** In this section, the problem of interest is a slender cantilever viscoelastic beam (Figure 1) submitted to free vibrations and satisfying the Euler-Bernoulli assumptions. Consequently, this study is limited to slender beams for which the transverse shear effects can be neglected. L denotes the length of the beam, W its width and h its thickness. The linear viscoelastic constitutive material may be represented by a classic generalized Maxwell model (Figure 2) [33] consisting in elementary Maxwell branches in parallel plus an elastic branch for the long-term elasticity.

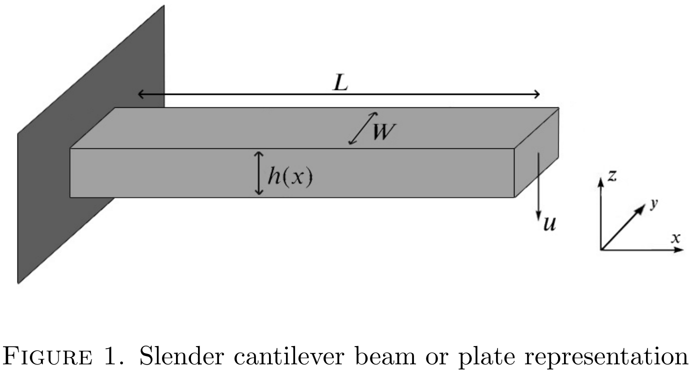

Figure 1. Slender cantilever beam or plate representation.

To introduce the model, let us first consider the three-dimensional (3D) bounded domain of the beam

$$\Omega^{3D} = \left\{ (x,y,z) \in \mathbb{R}^3 \mid x \in (0,L), y \in \left(\frac{-W}{2}, \frac{W}{2} \right), z \in \left(\frac{-h}{2}, \frac{h}{2} \right) \right\}. \tag{1}$$

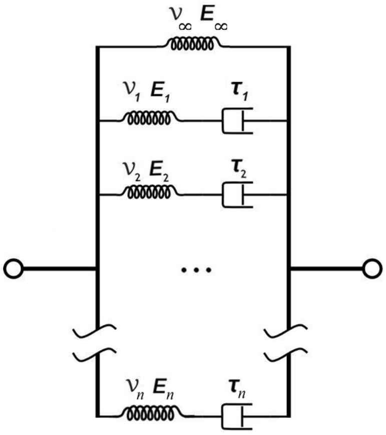

Figure 2. Generalized Maxwell rheological scheme.

During beam deformation, we assume small deformations. Here and throughout the paper, we focus on the out-of-plane displacement or deflection $U(x, y, z, t)$. With no external forces, it satisfies the principle of virtual power:

$$\int_{\Omega^{3D}} \rho \frac{\partial^2 U}{\partial t^2} \hat{u} dV + \int_{\Omega^{3D}} \sigma.\epsilon(\hat{u}) dV = 0 \qquad \forall t \in \mathbb{R}_+, \tag{2}$$

for all kinematically admissible $\hat{u}(x, y, z)$, where σ denotes the bending stress tensor, $\epsilon(\hat{u})$ is the bending infinitesimal strain tensor and ρ is the constant material density.

In the following, the slender beam is considered as a 1D structure, meaning that the only space variable for U and $\hat{u}$ is x, and its boundary is clamped at $x = 0$ and stress-free at $x = L$. For 1D problems the bending stress and strain simplify into scalars and satisfy the generalized Maxwell model (Figure 2) [35]:

$$\sigma(x, y, z, t) = E_\infty \epsilon(U)(x, y, z, t) + \sum_{j=1}^{n} E_j \int_{-\infty}^{t} e^{-\frac{t-\tau}{\tau_j}} \frac{\partial \epsilon(U)}{\partial \tau}(x, y, z, \tau) d\tau. \tag{3}$$

For slender beams the bending strain and virtual strain are expressed by

$$\epsilon(U)(x, y, z, t) = -z \frac{\partial^2 U}{\partial x^2}(x, t) \qquad \text{and} \qquad \epsilon(\hat{u})(x, y, z) = -z \frac{d^2 \hat{u}}{dx^2}(x). \tag{4}$$

Additionally, the solution U is assumed harmonic and writes as:

$$U(x, t) = u(x) e^{i\omega t}, \tag{5}$$

where the complex number ω stands for the system pulsation. Substituting $\epsilon(U)$ and U in (3), we obtain the bending stress as

$$\sigma(x, y, z, t) = -z e^{i\omega t} \left(E_\infty + \sum_{j=1}^{n} E_j \frac{i\omega\tau_j}{1 + i\omega\tau_j} \right) \frac{d^2 u}{dx^2}(x).$$

Substituting now σ, $\epsilon(\hat{u})$ and U in (2), the problem becomes: find $u \in \mathcal{U}_0$, such that

$$\int_0^L \frac{h^3}{12\rho} \frac{d^2 u}{dx^2} \frac{d^2 \hat{u}}{dx^2} dx = \frac{\omega^2}{E_\infty + \sum\limits_{j=1}^{n} E_j \frac{i\omega\tau_j}{1+i\omega\tau_j}} \int_0^L h u \hat{u} \, dx \qquad \forall \hat{u} \in \mathcal{U}_0, \tag{6}$$

with

$$\mathcal{U}_0 = \left\{ u \in H^2([0,L];\mathbb{C}) \mid u_{|x=0} = 0, \frac{du}{dx}_{|x=0} = 0 \right\}.$$

Standard arguments lead to the corresponding strong form:

$$(7)\qquad \begin{cases} \frac{1}{12\rho}\frac{d^2}{dx^2}(h^3\frac{d^2u}{dx^2}) = \frac{\omega^2}{E_\infty + \sum\limits_{j=1}^{n} E_j \frac{i\omega\tau_j}{1+i\omega\tau_j}} hu & \text{on } (0,L)\,, \\ u = 0 & \text{at } x=0, \\ \frac{du}{dx} = 0 & \text{at } x=0, \\ \frac{d^2u}{dx^2} = 0 & \text{at } x=L, \\ \frac{d}{dx}(h^3\frac{d^2u}{dx^2}) = 0 & \text{at } x=L. \end{cases}$$

The eigenpair (ω, u) is a solution of the above nonlinear eigenproblem in which $\omega \in \mathbb{C}$ and $u : [0,L] \to \mathbb{C}$. It is useful to note that this system can be simplified into a real linear eigenproblem by setting

$$(8)\qquad \lambda = \frac{\omega^2}{E_\infty + \sum\limits_{j=1}^{n} E_j \frac{i\omega\tau_j}{1+i\omega\tau_j}}.$$

Since this formulation involves a self-adjoint positive definite operator, its eigenvalues are positive real. Therefore, the complex pulsation ω is obtained by solving the real linear eigenproblem for the eigenvalue λ, then by solving the complex polynomial equation of degree $n+2$ resulting from (8). The pulsation of interest is selected within the set

$$F = \{\omega \in \mathbb{C} \mid \operatorname{Re}(\omega) > 0 \text{ and } \operatorname{Im}(\omega) > 0\}.$$

As the function $\lambda \mapsto \operatorname{Re}(\omega) \in F$ is monotonic, the pulsation corresponding to the first mode of vibration is obtained from the first eigenvalue of the linear eigenproblem in λ. For differentiability issues we further assume that this λ is simple, and the corresponding real and imaginary parts of the pulsation ω are denoted by

$$\omega_r = \operatorname{Re}(\omega), \qquad \omega_i = \operatorname{Im}(\omega).$$

2.2. **Objective function.** We aim at maximizing the damping of the beam free vibration. Several quantities characterizing the damping behavior of viscoelastic structures are reported in the literature and may be chosen as cost functions. Three options are discussed below.

First, a common quantity stands in the modal loss factor,

$$(9)\qquad \eta = \frac{\operatorname{Im}(\omega^2)}{\operatorname{Re}(\omega^2)} = \frac{2\omega_i\omega_r}{\omega_r^2 - \omega_i^2},$$

defining the ratio of the dissipated energy to the stored one [28, 21]. However, it may happen that the minimization simply leads to equalizing ω_r and ω_i. This phenomenon occurs more often when large thicknesses and shape variations are allowed or when the real and imaginary parts of the eigenfrequency are initially close. Therefore, η will be discarded.

Second, the vibration amplitude criterion defined by the logarithmic decrement as the ratio of the decay rate to the vibration frequency,

$$(10)\qquad \delta = \frac{\omega_i}{\omega_r},$$

is also used [31].

Finally, a third option is to focus on the decay rate of the vibration and directly use it as a cost function [4, 19],

$$\alpha = \omega_i. \tag{11}$$

In the following, the quantities δ and α will be considered as possible cost functions.

2.3. **Sizing optimization.** Our objective is to optimize the beam thickness profile in order to obtain the best damping properties. The cost function $\mathcal{J}(\lambda)$ writes as:

$$\mathcal{J}(\lambda) = -\frac{\omega_i(\lambda)}{\omega_r(\lambda)} \quad \text{or} \quad \mathcal{J}(\lambda) = -\omega_i(\lambda), \tag{12}$$

and it is also denoted by $\mathcal{J}(\lambda) = j(h)$ to highlight its dependence on the design variable h. Additionally, a volume constraint is applied on the structure and the minimization problem reads as:

$$\inf_{h \in \mathcal{H}_{ad}} j(h) \qquad \text{subject to} \qquad V(h) = \int_0^L h(x)dx = V_0, \tag{13}$$

where V_0 represents the initial volume of the beam and the set of admissible thickness profiles is

$$\mathcal{H}_{ad} = \left\{ h \in L^\infty(0,L) \mid h_{min} \leq h(x) \leq h_{max} \text{ in } [0,L] \right\}.$$

The computation of the first order derivative of the cost function with respect to the design variable is required to perform the numerical resolution of the optimization problem with a gradient method. We develop the procedure for $\mathcal{J}(\lambda) = -\frac{\omega_i(\lambda)}{\omega_r(\lambda)}$ only.

We recall that the Fréchet derivative of a function $f : E \subset X \to Y$, where X and Y are normed vector spaces, at a point h is a continuous linear map $Df(h) : X \to Y$ such that

$$\lim_{\|\tilde{h}\| \to 0} \frac{\|f(h+\tilde{h}) - f(h) - Df(h)\tilde{h}\|_Y}{\|\tilde{h}\|_X} = 0.$$

The partial Fréchet derivative with respect to h is denoted D_h. In the following we will extensively use standard differential calculus rules, as reported in classical textbooks.

The derivative of (6) with respect to h is first computed. For clarity the equation is denoted as

$$a(h,u,\hat{u}) = \lambda(h) b(h,u,\hat{u}) \qquad \forall \hat{u} \in \mathcal{U}_0,$$

with a and b bilinear in their second and third arguments, keeping in mind that u is also a function of h. Applying the chain rule yields

$$D_h a(h,u,\hat{u})\tilde{h} + a(h, D_h u\tilde{h}, \hat{u}) = D\lambda(h)\tilde{h} b(h,u,\hat{u}) + \lambda(h)\left(D_h b(h,u,\hat{u})\tilde{h} + b(h, D_h u \tilde{h}, \hat{u})\right) \qquad \forall \hat{u} \in \mathcal{W}_0.$$

Using the symmetry of a and b and choosing $\hat{u} = u$, we obtain

$$D_h a(h,u,u)\tilde{h} = D\lambda(h)\tilde{h} b(h,u,u) + \lambda(h) D_h b(h,u,u)\tilde{h},$$

whereby

$$D\lambda(h)\tilde{h} = \frac{D_h a(h,u,u)\tilde{h} - \lambda(h) D_h b(h,u,u)\tilde{h}}{b(h,u,u)}. \tag{14}$$

The application of the composite function rule to the cost function $j(h)$ using (14) provides the following expression,

$$Dj(h)\tilde{h} = -\frac{\omega_r\big(\lambda(h)\big)\frac{\partial \omega_i}{\partial \lambda}\big(\lambda(h)\big) - \omega_i\big(\lambda(h)\big)\frac{\partial \omega_r}{\partial \lambda}\big(\lambda(h)\big)}{\omega_r^2\big(\lambda(h)\big)} \int_0^L \left(\frac{1}{4\rho} h^2 \frac{\left(\frac{d^2u}{dx^2}\right)^2}{\int_0^L hu^2 dx} - \lambda(h) \frac{u^2}{\int_0^L hu^2 dx} \right) \tilde{h}\, dx.$$

The real and imaginary parts of the derivative of ω with respect to λ is found by rewritting (8) as

$$\omega^2 = \lambda \left(E_\infty + \sum_{j=1}^{n} E_j \frac{i\omega\tau_j}{1+i\omega\tau_j} \right),$$

which entails

$$2\omega\frac{d\omega}{d\lambda} = E_\infty + \sum_{j=1}^{n} E_j \frac{i\omega\tau_j}{1+i\omega\tau_j} + \lambda \sum_{j=1}^{n} E_j \left(\frac{i\tau_j}{1+i\omega\tau_j}\frac{d\omega}{d\lambda} + i\omega\tau_j \frac{-i\tau_j\frac{d\omega}{d\lambda}}{(1+i\omega\tau_j)^2} \right).$$

After simplification we arrive at

$$\frac{d\omega}{d\lambda} = \frac{E_\infty + \sum\limits_{j=1}^{n} E_j \frac{i\omega\tau_j}{1+i\omega\tau_j}}{2\omega - \lambda \sum\limits_{j=1}^{n} E_j \frac{i\tau_j}{(1+i\omega\tau_j)^2}},$$

and we infer $\frac{d\omega_r}{d\lambda} = \mathrm{Re}\left(\frac{d\omega}{d\lambda}\right)$ and $\frac{d\omega_i}{d\lambda} = \mathrm{Im}\left(\frac{d\omega}{d\lambda}\right)$.

This paper is limited to eigenvalue optimization problems which are self-adjoint, the work could be extended to other objective functions through the construction and resolution of the adjoint problem.

2.4. **Numerical methods.** The bending problem of a viscoelastic cantilever beam is a fourth-order problem set in a subspace of $H^2(0,L)$, hence conforming finite elements need to be $\mathcal{C}^1$. This $\mathcal{C}^1$ continuity is a rather strong restriction and causes some computational difficulties as the finite element space has a more complex structure and a significantly larger dimension compared with $\mathcal{C}^0$ elements. In this 1D problem we bypass this difficulty with the help of a mixed formulation.

The mixed formulation is based on the introduction of the additional variable $v = -\frac{h^3}{12\rho}\frac{d^2u}{dx^2}$, with the help of which the strong form (7) can be rewritten as

$$\begin{cases} -\frac{d^2v}{dx^2} = \lambda h u & \text{on } (0,L)\,, \\ -\frac{d^2u}{dx^2} = 12\rho h^{-3} v & \text{on } (0,L)\,, \\ u = 0 & \text{at } x=0, \\ v = 0 & \text{at } x=L, \\ \frac{du}{dx} = 0 & \text{at } x=0, \\ \frac{dv}{dx} = 0 & \text{at } x=L. \end{cases}$$

Setting

$$\mathcal{U}_1 = \left\{ (u,v) \in H^1([0,L],\mathbb{C}) \times H^1([0,L],\mathbb{C}) \mid u_{|x=0} = 0, v_{|x=L} = 0 \right\},$$

we have the corresponding variational formulation: find $(u,v) \in \mathcal{U}_1$, such that

$$\text{(15)} \qquad \begin{cases} \int_0^L \frac{dv}{dx}\frac{d\hat{u}}{dx}dx = \lambda \int_0^L h u \hat{u}\, dx \\ \int_0^L \frac{du}{dx}\frac{d\hat{v}}{dx}dx - \int_0^L 12\rho h^{-3} v\hat{v}\, dx = 0 \end{cases} \qquad \forall (\hat{u},\hat{v}) \in \mathcal{U}_1.$$

All algorithms discussed in this paper were implemented in FreeFem++ [22], an open-source PDE solver using the finite element method. In the mixed formulation the eigenfunction belongs to H^1, therefore the problem can be solved with usual finite elements such as classic P_1 elements. The linear eigenproblem is solved using the ARPACK library included in FreeFem++, and the roots of the complex polynomial arising from (8) are found using Python polynomial solvers from the library PyFreeFem for the Python/FreeFem++ interface.

The optimization problem is solved using the steepest descent method with line search. Moreover, the gradient is regularized using the H^1 inner product to prevent "checkerboards" irregularities [1]. The thickness h now belongs to the regularized set of admissible thickness profiles

$$\mathcal{H}_{ad}^{reg} = \left\{ h \in H^1(0,L) \mid h_{min} \leq h(x) \leq h_{max} \text{ in } [0,L] \right\},$$

and the gradient $j'(h)$ is identified through

$$\langle j'(h), \tilde{h} \rangle_{H^1} = Dj(h)\tilde{h} \qquad \forall \tilde{h} \in H^1(0,L),$$

using the H^1 inner product

$$\langle j'(h), \tilde{h} \rangle_{H^1} = \int_0^L \left(\eta^2 \frac{dj'(h)}{dx} \frac{d\tilde{h}}{dx} + j'(h)\tilde{h} \right) dx$$

where η is to be interpreted as a regularization length-scale of the order of a mesh cell size.

The box and volume constraints are enforced by projection. The projection operator onto $\mathcal{H}_{ad}^{reg}$ is approximated by the projection onto $\mathcal{H}_{ad}$ given by

$$\big(P_{ad}(h)\big)(x) = max\left(h_{min}, min(h_{max}, h(x) + \ell)\right),$$

where ℓ is determined by bisection such that $\int_0^L P_{ad}(h)dx = V_0$, using the monotonicity of the function

$$\ell \to V(\ell) = \int_0^L max\left(h_{min}, min(h_{max}, h(x) + \ell)\right) dx.$$

This projection method ensures that the constraints are satisfied at each iteration.

A 200 × 1 mesh is used to solve the problem. Finer meshes have shown to provide similar results. The optimization algorithm stops when the relative change of the objective function $\frac{\mathcal{J}_n - \mathcal{J}_{n+1}}{\mathcal{J}_{n+1}}$, where $\mathcal{J}_n$ is the value of the objective function at iteration n, reaches a small enough value $\xi_0 = 10^{-4}$.

2.5. **Materials of interest.** Polymers are good candidates for damped oscillation applications as they show linear viscoelastic properties at infinitesimal strain that can be tailored according to the physics and chemistry of the polymers. Their linear viscoelasticity may be simply characterized by dynamic mechanical analysis in torsion or in uniaxial tension. The sinusoidal mechanical tests give access to either the shear or the Young's storage and loss moduli with respect to the applied frequency. The generalized Maxwell model parameters (Figure 2) are then obtained by a mere fit of the experimental data. In order to run simulations close to realistic applications, we consider generalized Maxwell model parameters fit on the linear viscoelastic behavior measured in tension of an actual amorphous acrylate network (Figure 3) [14]. The model is characterized by the set of parameters table 1. For later plate vibration applications, the bulk modulus K may be assumed elastic constant equal to 3000 MPa. While this assumption is not strictly correct, it is often made [11, 10] since the viscoelasticity of polymers upon hydrostatic loadings is very difficult to measure experimentally, and while the Young's modulus drops of about three order of magnitude from the high to the low frequencies, the bulk modulus changes from a factor two or three only [8]. With this assumption, the frequency dependent Poisson's ratio can be simply calculated, $\nu_j = \frac{3K - E_j}{6K}$ [34].

Note that in general several relaxation times τ_j are required to provide an accurate representation of the linear viscoelasticity of an actual polymer. This renders difficult the study of the impact of material parameters on the presented results. Therefore, the simpler Zener model consisting in only one Maxwell viscous branch

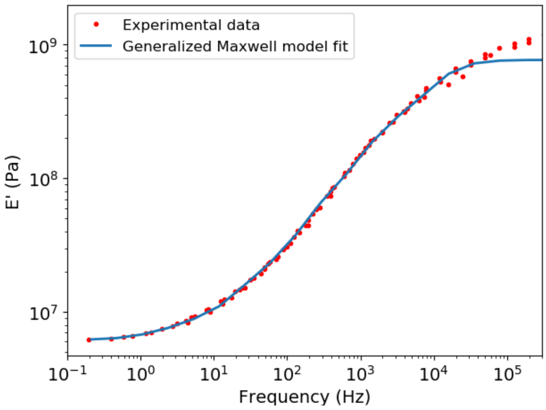

FIGURE 3. Storage modulus master curve and generalized Maxwell model fit for an acrylate polymer network.

$E_\infty = 6.2$ MPa	
E_j (MPa)	τ_j (s)
4.761×10^2	1.396×10^{-7}
2.126×10^2	1.054×10^{-6}
58.665	7.231×10^{-6}
12.255	6.001×10^{-5}
2.012	4.526×10^{-4}
7.866×10^{-1}	1.582×10^{-3}

TABLE 1. Generalized Maxwell model parameters used to fit experimental data

in parallel with an elastic branch will also be considered, limiting the model parameters to E_∞, E_1, τ_1 for the beam, added of ν_∞ and ν_1 for the plate.

2.6. **Results.** First, the thickness profile of a cantilever beam of initial thickness h_0, density $\rho = 1000 kg.m^{-3}$ and mechanical properties described Figure 3, is optimized for $\mathcal{J}(\lambda) = -\frac{\omega_i(\lambda)}{\omega_r(\lambda)}$. The final thickness profile as well as the free vibration amplitudes of the beam for $L = 60mm$ and an initial displacement at the free end $u_0 = 3mm$ are given and compared to their initial counterparts in Figure 4. The best geometry redistributes the material from the free end to the clamped end of the beam, saturating the bounds. The optimized beam shows a significant increase in damping compared to the initial beam asserting the relevance of the method. The good performance of the algorithm can be observed on the objective function convergence displayed in Figure 5.

In order to study the impact of the material properties on the optimization, the Zener model is now used. The reference material parameters are conveniently chosen to $E_\infty = 18$ MPa, $E_1 = 30$ MPa and $\tau_1 = 0.001$ s in order to witness some damping. By increasing E_∞, the material tends toward an elastic material, therefore the damping of the structure decreases. On the contrary, increasing E_1, the modulus of the viscoelastic branch, increases the damping. These tendencies are noticeable when comparing different initial beams as well as when comparing

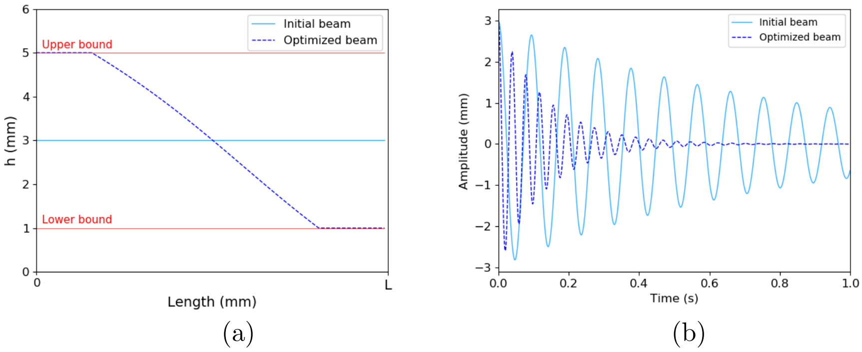

(a) (b)

FIGURE 4. (a) Thickness profiles of the initial and optimized beams and (b) free vibration amplitudes of the considered beams at $x = L$ for material parameters listed in table 1.

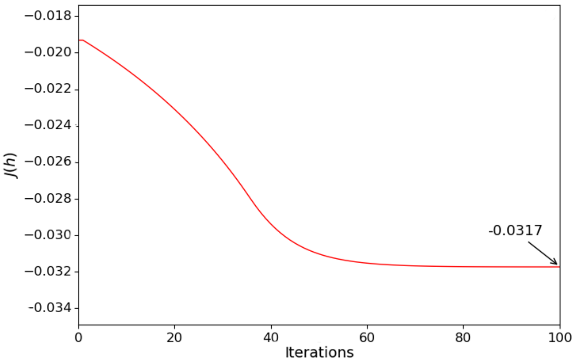

FIGURE 5. Cost function convergence with respect to the number of iterations for the damping optimization of the generalized Maxwell rectangular beam.

the optimized beams without affecting significantly the final thickness profile or the optimization efficiency. When the relaxation time τ_1 tends to zero or to infinity the material behaves as a purely elastic material, these cases stray away from the purpose of the algorithm. Figure 6 shows the final thickness profile as well as the free vibration amplitudes of the beam for different values of τ_1. The thickness profile and the free vibration amplitudes of the optimized beams are considerably different especially for high values of τ_1, Figure 6 (b). In this case the material is distributed at the free end of the beam, similarly to a pendulum, decreasing both the exponential decay rate and the frequency (respectively the numerator and denominator of the cost function).

Contrastingly, the maximization of the decay rate α instead of δ leads to the same optimized thickness profile similar to Figure 4 (a), independently of the material parameters, assessing δ as the most interesting cost function.

3. OPTIMIZATION OF VISCOELASTIC PLATES UNDER FREE VIBRATION

3.1. Plate free vibration problem.

The free vibration of thin plates satisfying the Kirchhoff-Love assumptions is now of interest. Accordingly, both transversal

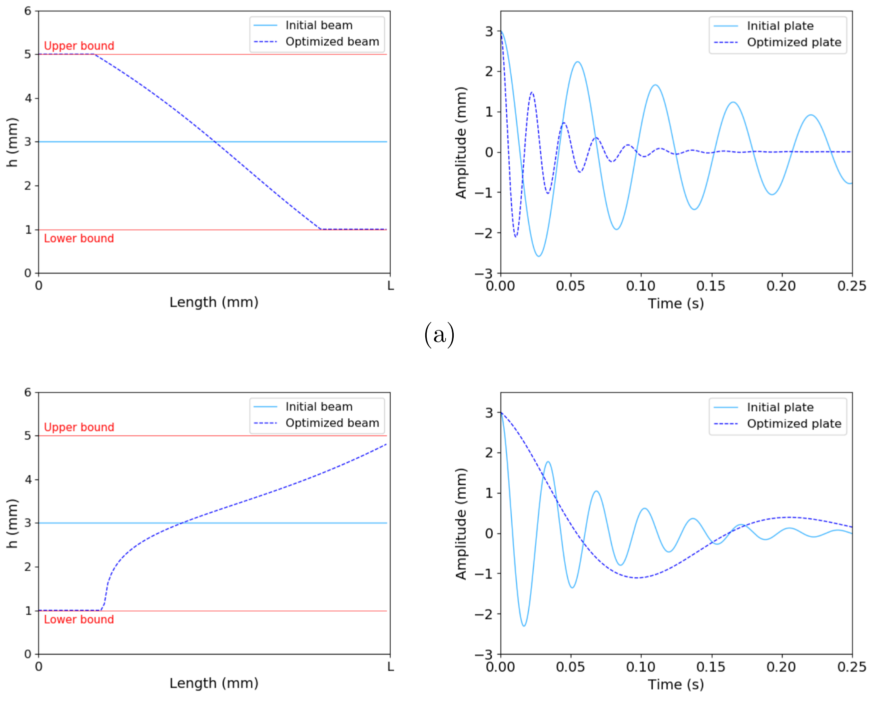

(a)

(b)

FIGURE 6. Impact of the relaxation time on the thickness profile and free vibration amplitudes of optimized beams for a Zener material of same Young's moduli $E_\infty = 18$ MPa, $E_1 = 30$ MPa and different relaxation times (a) $\tau_1 = 0.0005$ s - (b) $\tau_1 = 0.02$ s.

shear and normal strains are neglected. The working domain is now the midsurface of the 3D plate defined by

$$\Omega = \left\{ (x, y) \in \mathbb{R}^2 \mid x \in (0, L), y \in \left(\frac{-W}{2}, \frac{W}{2} \right) \right\}. \tag{16}$$

Dirichlet conditions are applied on the clamped part denoted Γ_D at $x = 0$ and stress-free Neumann conditions are applied on the remaining boundaries denoted Γ_N. The isotropic material behavior representation as a generalized Maxwell model remains. The state equation (2) is adapted to the 2D case where $U(x, y, t)$ represents the plate deflection. We still consider small deformations. Note that due to the plate structure, the free vibration is now not only dependent on Young's modulus E but also on Poisson's ratio ν. Adapting (3) to the 2D case, the linear plane strain tensor $\epsilon(U)$ is expressed as the 3-component vector

$$\epsilon(U)(x, y, z, t) = \begin{pmatrix} \epsilon_1 \\ \epsilon_2 \\ \gamma_{12} \end{pmatrix} = \begin{pmatrix} -z\dfrac{\partial^2 U}{\partial x^2} \\ -z\dfrac{\partial^2 U}{\partial y^2} \\ -2z\dfrac{\partial^2 U}{\partial x \partial y} \end{pmatrix},$$

and the scalar displacement $U(x, y, t)$, with $(x, y) \in \Omega$, writes for the free vibration of the plate as

$$U(x, y, t) = u(x, y)e^{i\omega t}.$$

The bending plane stress tensor is given by

$$\sigma(x,y,z,t) = C_\infty \epsilon(U)(x,y,z,t) + \int_{-\infty}^{t} R(t-\tau)\frac{\partial \epsilon(U)}{\partial \tau}(x,y,z,\tau)d\tau,$$

where the first term represents the relaxed stress with C_∞ the second-order stiffness tensor at equilibrium, and the second term represents the stress history with R the second-order tensor of relaxation function. They are expressed as

$$C_\infty = \begin{pmatrix} \frac{E_\infty}{1-\nu_\infty^2} & \nu_\infty \frac{E_\infty}{1-\nu_\infty^2} & 0 \\ \nu_\infty \frac{E_\infty}{1-\nu_\infty^2} & \frac{E_\infty}{1-\nu_\infty^2} & 0 \\ 0 & 0 & \frac{E_\infty}{2(1+\nu_\infty)} \end{pmatrix}, \quad R(\tau) = \sum_{j=1}^{n} \begin{pmatrix} \frac{E_j}{1-\nu_j^2} & \nu_j \frac{E_j}{1-\nu_j^2} & 0 \\ \nu_j \frac{E_j}{1-\nu_j^2} & \frac{E_j}{1-\nu_j^2} & 0 \\ 0 & 0 & \frac{E_j}{2(1+\nu_j)} \end{pmatrix} e^{-\frac{\tau}{\tau_j}}.$$

After integration by parts the expression becomes

$$\sigma(x,y,z,t) = C_0 \epsilon(U)(x,y,z,t) + \int_{-\infty}^{t} \frac{\partial R}{\partial \tau}(t-\tau)\epsilon(U)(x,y,z,\tau)d\tau, \tag{17}$$

where the first term represents the instantaneous response by

$$C_0\epsilon(U)(x,y,z,t) = \begin{bmatrix} c_{11} & c_{12} & 0 \\ c_{12} & c_{22} & 0 \\ 0 & 0 & c_{33} \end{bmatrix} \begin{pmatrix} \epsilon_1 \\ \epsilon_2 \\ \gamma_{12} \end{pmatrix} \text{ with } \begin{cases} c_{11} = c_{22} = \frac{E_\infty}{1-\nu_\infty^2} + \sum_{j=1}^{n} \frac{E_j}{1-\nu_j^2}, \\ c_{12} = \nu_\infty \frac{E_\infty}{1-\nu_\infty^2} + \sum_{j=1}^{n} \nu_j \frac{E_j}{1-\nu_j^2}, \\ c_{33} = \frac{E_\infty}{2(1+\nu_\infty)} + \sum_{j=1}^{n} \frac{E_j}{2(1+\nu_j)}. \end{cases}$$

The second term reads

$$\int_{-\infty}^{t} \frac{\partial R}{\partial \tau}(t-\tau)\epsilon(U)(x,y,z,\tau)d\tau = -\int_{-\infty}^{t} \begin{bmatrix} r_{11} & r_{12} & 0 \\ r_{12} & r_{22} & 0 \\ 0 & 0 & r_{33} \end{bmatrix} \begin{pmatrix} \epsilon_1 \\ \epsilon_2 \\ \gamma_{12} \end{pmatrix} d\tau \text{ with } \begin{cases} r_{11} = r_{22} = \sum_{j=1}^{n} \frac{E_j}{(1-\nu_j^2)\tau_j} e^{\frac{\tau-t}{\tau_j}}, \\ r_{12} = \sum_{j=1}^{n} \frac{\nu_j E_j}{(1-\nu_j^2)\tau_j} e^{\frac{\tau-t}{\tau_j}}, \\ r_{33} = \sum_{j=1}^{n} \frac{E_j}{2(1+\nu_j)\tau_j} e^{\frac{\tau-t}{\tau_j}}, \end{cases}$$

which becomes in the frequency domain

$$\int_{-\infty}^{t} \frac{\partial R}{\partial \tau}(t-\tau)\epsilon(U)(x,y,z,\tau)d\tau = \begin{bmatrix} \tilde{r}_{11} & \tilde{r}_{12} & 0 \\ \tilde{r}_{12} & \tilde{r}_{22} & 0 \\ 0 & 0 & \tilde{r}_{33} \end{bmatrix} \begin{pmatrix} z\frac{\partial^2 u}{\partial x^2} \\ z\frac{\partial^2 u}{\partial y^2} \\ 2z\frac{\partial^2 u}{\partial x \partial y} \end{pmatrix} e^{i\omega t} \text{ with } \begin{cases} \tilde{r}_{11} = \tilde{r}_{22} = \sum_{j=1}^{n} \frac{E_j}{(1+i\omega\tau_j)(1-\nu_j^2)}, \\ \tilde{r}_{12} = \sum_{j=1}^{n} \nu_j \frac{E_j}{(1+i\omega\tau_j)(1-\nu_j^2)}, \\ \tilde{r}_{33} = \sum_{j=1}^{n} \frac{E_j}{2(1+i\omega\tau_j)(1+\nu_j)}. \end{cases}$$

The set of kinematically admissible displacements is defined by

$$\mathcal{U}_2 = \left\{ u \in H^2(\Omega,\mathbb{C}) \mid u_{|\Gamma_D} = 0, \frac{du}{dn}_{|\Gamma_D} = 0 \right\}. \tag{18}$$

Given $u, \hat{u} \in \mathcal{U}_2$, the expressions of σ and $\epsilon(\hat{u})$ are substituted in (2), and after explicit integration with respect to z, one obtains the spatial equation:

$$-\omega^2 \rho h \int_\Omega u\hat{u}\, dA + \frac{h^3}{12}\int_\Omega \Bigg((c_{11}-\tilde{r}_{11})\left(\frac{\partial^2 u}{\partial x^2}\frac{\partial^2 \hat{u}}{\partial x^2} + \frac{\partial^2 u}{\partial y^2}\frac{\partial^2 \hat{u}}{\partial y^2}\right) + (c_{12}-\tilde{r}_{12})\left(\frac{\partial^2 u}{\partial x^2}\frac{\partial^2 \hat{u}}{\partial y^2} + \frac{\partial^2 u}{\partial y^2}\frac{\partial^2 \hat{u}}{\partial x^2}\right)$$
$$+ 2\,(c_{33}-\tilde{r}_{33})\,\frac{\partial^2 u}{\partial x \partial y}\frac{\partial^2 \hat{u}}{\partial x \partial y}\Bigg) dA = 0.$$

This equation is then rewritten as a complex polynomial eigenproblem of form

$$\sum_{j=0}^{n+2} \omega^j a_j(h, u, \hat{u}) = 0 \qquad \forall \hat{u} \in \mathcal{U}_2, \tag{19}$$

where the pulsation ω denotes the complex eigenvalue of the vibration problem and a_j are complex symmetric bilinear forms independent of ω, explicitly given in Appendix A. Note that when Poisson's ratio is identical in every Maxwell branch, (19) may be factorized similarly to the beam case and simply solved as a real linear eigenproblem followed by a complex polynomial root-finding problem. However, considering a constant elastic bulk modulus yields a frequency dependent Poisson's ratio, introducing non-linearity in the eigenproblem. Consequently, this factorization is no longer valid as the relation between the strain and stress tensors is less straightforward. The general case is considered in what follows.

3.2. **Coupled optimization.** This subsection is focused on the coupled optimization of the shape and thickness of a thin rectangular plate modeled by the generalized Maxwell model. The design parameters are $(h, \Omega) \in \mathcal{H}_{ad} \times \mathcal{U}_{ad}$. The clamped boundary Γ_D is fixed while the position of the free boundary Γ_N is subject to optimization. An inner shape denoted by Ω_f is fixed in the working domain as a geometrical constraint, see Figure 7. The main purpose of this constraint is to prevent possible trivial results with accumulated material at the clamped boundaries, usually in the form of circular shapes, which may be less interesting for potential applications. The set of admissible shapes $\mathcal{U}_{ad}$ is then defined by

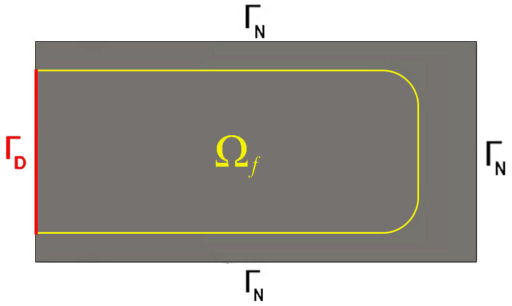

FIGURE 7. Representation of the initial plate with the geometric constraint.

$$\mathcal{U}_{ad} = \left\{\Omega \in \mathbb{R}^2 \mid \Gamma_D \subset \partial\Omega, \Omega_f \subset \Omega\right\},$$

while the set of admissible thickness profiles becomes

$$\mathcal{H}_{ad} = \{h \in L^\infty(\Omega) \mid h_{min} \leq h(x, y) \leq h_{max} \text{ in } \Omega\}.$$

For this problem the complex pulsation $\omega = \omega_r + i\omega_i$ depends implicitly on h and Ω. Using the logarithmic decrement as cost function

$$\mathcal{J}(h, \Omega) = -\frac{\omega_i(h, \Omega)}{\omega_r(h, \Omega)} \tag{20}$$

and the volume constraint, the minimization problems reads:

$$\inf_{(h,\Omega) \in \mathcal{H}_{ad} \times \mathcal{U}_{ad}} \mathcal{J}(h, \Omega) \qquad \text{subject to} \qquad V(h, \Omega) = \int_\Omega h(x, y) dA = V_0. \tag{21}$$

3.2.1. *Sizing optimization.* The proposed resolution method is a coupled optimization alternating sizing and shape optimization, both using a gradient algorithm. The sizing optimization is performed using the derivative of $\mathcal{J}$ with respect to the thickness. In this subsection the shape Ω is fixed and the pulsation is denoted $\omega(h)$.

The derivative of (19) is first established. As each a_j is a bilinear form we obtain

$$\sum_{j=0}^{n+2} j\omega(h)^{j-1}D\omega(h)\tilde{h}\ a_j(h,u,\hat{u})+\omega(h)^j\Big(D_h a_j(h,u,\hat{u})\tilde{h}+a_j(h,D_h u\tilde{h},\hat{u})\Big)=0 \quad \forall \hat{u}\in\mathcal{U}_2.$$

Using the symmetry of a_j and chosing $\hat{u}=u$ we arrive at

$$\sum_{j=0}^{n+2} j\omega(h)^{j-1}D\omega(h)\tilde{h}\ a_j(h,u,u)+\omega(h)^j D_h a_j(h,u,u)\tilde{h}=0,$$

whence

$$D\omega(h)\tilde{h}=-\frac{\sum\limits_{j=0}^{n+2}\omega(h)^j D_h a_j(h,u,u)\tilde{h}}{\sum\limits_{j=1}^{n+2} j\omega(h)^{j-1}a_j(h,u,u)}. \tag{22}$$

Using the expression of the bilinear forms as $a_j(h,u,\hat{u})=\int_\Omega g_j(h(x),u(x),\hat{u}(x))dA$, (22) can be rewritten in the form

$$D\omega(h)\tilde{h}=\int_\Omega W(h,u,u)\tilde{h}\,dA, \qquad W(h,u,u)\tilde{h}=-\frac{\sum\limits_{j=0}^{n+2}\omega(h)^j D_h g_j(h,u,u)\tilde{h}}{\sum\limits_{j=1}^{n+2} j\omega(h)^{j-1}a_j(h,u,u)}, \tag{23}$$

where the duality pairing $D_h g_j(h,u,u)\tilde{h}$ is simply an algebraic product. The chain rule applied to the cost function $\mathcal{J}(h)$ provides the expression

$$D\mathcal{J}(h)\tilde{h}=-\frac{\omega_r(h)D\omega_i(h)\tilde{h}-\omega_i(h)D\omega_r(h)\tilde{h}}{\omega_r(h)^2}. \tag{24}$$

Plugging (23) into (24) yields

$$D\mathcal{J}(h)\tilde{h}=\int_\Omega -\frac{\omega_r(h)\operatorname{Im}\big(W(h,u,u)\big)-\omega_i(h)\operatorname{Re}\big(W(h,u,u)\big)}{\omega_r(h)^2}\tilde{h}\,dA, \tag{25}$$

from which the gradient relatively to the L^2-inner product is immediately inferred.

3.2.2. *Shape optimization.* Shape optimization is performed by means of the concept of shape derivative. We use the framework of Murat-Simon [32] following the spirit of Hadamard's method, see also [1, 23]. Given a reference domain Ω, we consider the perturbed domain

$$\Omega_\theta=(Id+\theta)\Omega \qquad \text{with} \qquad \theta\in W^{1,\infty}(\mathbb{R}^2,\mathbb{R}^2).$$

This θ can be seen as a (bounded and Lipschitz) vector field advecting the reference domain. For any θ small enough in the norm of $W^{1,\infty}(\mathbb{R}^2,\mathbb{R}^2)$ the map $(Id+\theta)$ is a bijection of $\mathbb{R}^2$.

Definition 3.1. *The shape derivative of a functional $F(\Omega_\theta)$ at Ω is the Fréchet derivative of the mapping $\theta\mapsto F((Id+\theta)\Omega)$ at $\theta=0$ which can be expressed as follows:*

$$F((Id+\theta)\Omega)=F(\Omega)+D_\Omega F(\Omega)\theta+o(\theta) \qquad \textit{with} \qquad \lim_{\theta\to 0}\frac{|o(\theta)|}{\|\theta\|_{W^{1,\infty}}}=0$$

for all $\theta \in W^{1,\infty}(\mathbb{R}^2, \mathbb{R}^2)$*, where* $D_\Omega F(\Omega)$ *is a continuous linear form on* $W^{1,\infty}(\mathbb{R}^2, \mathbb{R}^2)$ *called the shape derivative of* F*.*

We recall a classical result on the shape derivatives, see [1] for a proof.

Lemma 3.1. *Given* $f \in W^{1,1}(\mathbb{R}^2)$*, consider the functional*

$$F(\Omega) = \int_\Omega f(x) dA.$$

Then F *is shape differentiable at* Ω *and its shape derivative is*

$$D_\Omega F(\Omega)\theta = \int_\Omega \operatorname{div}\big(\theta(x) f(x)\big) dA = \int_{\partial\Omega} f(s)\theta(s).n(s) ds.$$

Before computing the shape derivative in the present context, the evolution of the thickness during the shape optimization has to be specified. Following the framework of [20], the thickness profile h will be transported by the same diffeomorphism while deforming the shape:

$$h_\theta = h \circ (Id + \theta)^{-1}.$$

The cost function is now denoted by

$$j(\Omega) = \mathcal{J}(h_\theta, \Omega),$$

and for the sake of clarity the pulsation $\omega(h_\theta, \Omega)$ is simply denoted ω. The problem (19) is rewritten as

$$\sum_{j=0}^{n+2} \omega^j a_j(h, \Omega, u, \hat{u}) = 0 \qquad \forall \hat{u} \in \mathcal{U}_2,$$

where the complex symmetric bilinear forms are expressed as

$$a_j(h, \Omega, u, \hat{u}) = \int_\Omega g_j(h, u, \hat{u}) dA \quad \forall j \in [\![0, n+2]\!].$$

Proposition 3.1. *For any* $\theta \in W^{1,\infty}(\mathbb{R}^2, \mathbb{R}^2)$ *such that* $\theta = 0$ *on* Γ_D *and* $\Omega_f \subset \Omega$*, the shape derivative of* $j(\Omega)$ *is given by*

$$\begin{aligned} D_\Omega j(\Omega)\theta = &- \int_{\Gamma_N} \frac{\omega_r \operatorname{Im}\big(f(\omega, h, u)\big) - \omega_i \operatorname{Re}\big(f(\omega, h, u)\big)}{\omega_r^2} \theta.n \, ds \\ &+ \int_\Omega \frac{\omega_r D_h \omega_i - \omega_i D_h \omega_r}{\omega_r^2} \theta.\nabla h \, dA, \end{aligned} \tag{26}$$

where $f(\omega, h, u)$ *is defined by*

$$f(\omega, h, u) = -\frac{\sum\limits_{j=0}^{n+2} \omega^j g_j(h, u, u)}{\sum\limits_{j=1}^{n+2} j\omega^{j-1} a_j(h, \Omega, u, u)}. \tag{27}$$

Proof. Using the chain rule and the linearity of a_j, the derivative of problem (19) with respect to the shape with u and $\hat{u}$ fixed, following the spirit of Céa's method [9], writes as:

$$\sum_{j=0}^{n+2} j\omega^{j-1} D_\Omega\omega\theta \; a_j(h, \Omega, u, \hat{u}) + \omega^j \Big(D_\Omega a_j(h, \Omega, u, \hat{u})\theta + a_j(h, \Omega, D_\Omega u\theta, \hat{u}) \Big) = 0 \quad \forall \hat{u} \in \mathcal{U}_2.$$

By symmetry of a_j and chosing $\hat{u} = u$ we obtain

$$\sum_{j=0}^{n+2} j\omega^{j-1} D_\Omega\omega\theta\, a_j(h,\Omega,u,u) + \omega^j D_\Omega a_j(h,\Omega,u,u)\theta = 0,$$

thence

$$D_\Omega\omega\theta = -\frac{\sum\limits_{j=0}^{n+2} \omega^j D_\Omega a_j(h,\Omega,u,u)\theta}{\sum\limits_{j=1}^{n+2} j\omega^{j-1} a_j(h,\Omega,u,u)}.$$

By applying Lemma 3.1 the shape derivative of ω is expressed as:

$$D_\Omega\omega\theta = \int_{\Gamma_N} -\frac{\sum\limits_{j=0}^{n+2} \omega^j g_j(h,u,u)}{\sum\limits_{j=1}^{n+2} j\omega^{j-1} a_j(h,\Omega,u,u)}\theta.n\,ds = \int_{\Gamma_N} f(\omega,h,u)\theta.n\,ds. \tag{28}$$

For small θ the Taylor expansion of $\theta \mapsto h_\theta$ reads

$$h_\theta = h \circ (Id+\theta)^{-1} = h - \theta.\nabla h + o(\theta),$$

the shape derivative of the cost function then writes as

$$D_\Omega j(\Omega)\theta = D_\Omega \mathcal{J}(h,\Omega)\theta - \int_\Omega D_h\mathcal{J}(h,\Omega)\theta.\nabla h\, dA.$$

The chain rule now yields

$$D_\Omega j(\Omega)\theta = -\frac{\omega_r D_\Omega\omega_i - \omega_i D_\Omega\omega_r}{\omega_r^2}\theta + \int_\Omega \frac{\omega_r D_h\omega_i - \omega_i D_h\omega_r}{\omega_r^2}\theta.\nabla h\, dA.$$

Substituting the shape derivative of ω using (28), we obtain the claim. □

Following the same method, the shape derivative of the volume $v(\Omega) = \int_\Omega h_\theta(x)dA$ is found as

$$D_\Omega v(\Omega)\theta = \int_\Gamma h\theta.nds - \int_\Omega \theta.\nabla\, hdA. \tag{29}$$

3.3. **Numerical methods.** The bending problem of a viscoelastic cantilever plate is a fourth-order problem, however in 2D the mixed formulation requires considerable additional work [30]. Here non-conforming Morley elements are used for the resolution of the variational formulation. In order to solve the complex polynomial eigenproblem (19), we employ polynomial eigensolvers from the library SLEPc [24] which has been specifically interfaced with FreeFem++ for this study.

The general procedure for the coupled optimization is to alternatively optimize the thickness and the shape, both by gradient descent using line search. The thickness h is updated at each iteration using the previously introduced method and the shape Ω is updated every m iterations using the Hadamard's boundary variation method as well as the mesh deformation method. Changing m affects the convergence rate but can also lead to different local minima, the shown results have been obtained with $m = 3$ which seemed to be the most efficient. Contrary to the beam case, the coupled optimization of plates is prone to local minima issues. Several optimizations with different initializations have been performed and compared for each result to reduce the possibility of suboptimal designs. A 100x50 structured triangular mesh is used for the numerical resolution of the sizing optimization problem and a 100x50 unstructured triangular mesh is used for the shape and coupled optimizations. Similar results are obtained for finer meshes.

In order to deform the mesh the displacement field $\theta \in H^1(\Omega, \mathbb{R}^2)$ advecting the shape is constructed from the linear combination of the shape derivative of the cost function (26) and the shape derivative of the volume (29):

$$D_\Omega (j + \ell v)(\Omega)\theta = \int_{\Gamma_N} \left(-\frac{\omega_r \operatorname{Im}\big(f(\omega, h, u)\big) - \omega_i \operatorname{Re}\big(f(\omega, h, u)\big)}{\omega_r^2} + \ell h \right) \theta . n \, ds + \int_\Omega \left(\frac{\omega_r D_h \omega_i - \omega_i D_h \omega_r}{\omega_r^2} - \ell \right) \theta . \nabla h \, dA, \tag{30}$$

where ℓ is the Lagrange multiplier associated with the volume constraint and f has been defined in (27). Simple ideas to determine the advection field could be used where θ is not only defined on the boundaries but also inside the shape as mentioned in [20]. While this allows less frequent remeshing compared to an advection field defined only on the boundaries, it results in the discontinuity of θ at the boundaries, which represents a major drawback. Therefore, a regularization of θ is performed increasing the smoothness of the solution and avoiding potential boundary oscillations. We again rely on a regularization through the H^1 inner product by

$$\int_\Omega (\eta^2 \nabla\theta \cdot \nabla\hat{\theta} + \theta \cdot \hat{\theta}) dA = -D_\Omega (j + \ell v)(\Omega)\hat{\theta} \qquad \forall \hat{\theta} \in H^1(\Omega), \tag{31}$$

which implies that the advection field θ is then solution of the following system:

$$\begin{cases} -\eta^2 \Delta\theta + \theta = \left(-\frac{\omega_r D_h \omega_i - \omega_i D_h \omega_r}{\omega_r^2} + \ell \right) \nabla h & \text{in } \Omega \\ \theta = 0 & \text{on } \Gamma_D \\ \eta^2 \frac{\partial \theta}{\partial n} = \left(\frac{\operatorname{Im}\big(f(\omega)\big)\omega_r - \omega_i \operatorname{Re}\big(f(\omega)\big)}{\omega_r^2} - \ell h \right) n & \text{on } \Gamma_N. \end{cases} \tag{32}$$

Here the regularization parameter η is of the order of a mesh cell size. Finally, the whole mesh is deformed by the advection field θ solution of (32) and a remeshing is performed at each update of the shape to ensure a better mesh quality. The smoothness of θ enables less frequent remeshing, reducing the computational cost. The constraints are applied by projecting h and θ on the admissible sets $\mathcal{H}_{ad}$ and $\mathcal{U}_{ad}$ respectively, noting that the latter merely consists in adjusting the Lagrange multiplier ℓ.

In this work, thermoset polymers have been considered since E_∞ has been chosen different from zero. One could also apply the optimization problem to viscous thermoplastics. In this case E_∞ is null and so is a_0, the term of degree zero of the polynomial eigenproblem, which can be an issue for the convergence of the eigensolver. A mere factorization by ω performed beforehand reduces the degree of the polynomial by one and considerably increases the accuracy of the solver.

3.4. **Results.**

3.4.1. *Sizing optimization.* First, the sizing optimization of several viscoelastic cantilever plates is performed. The bulk modulus is constant, $L = 60mm$ and $W = 30mm$. The final thickness profile of the optimized plate as well as its free vibration amplitude are shown and compared to those of the initial plate in Figure 8. Similarly to the beam case, the material is distributed at the clamped end of the plate, increasing the logarithmic decrement of vibration significantly. The cost function converges, validating the algorithm efficiency as displayed in Figure 9. Note that

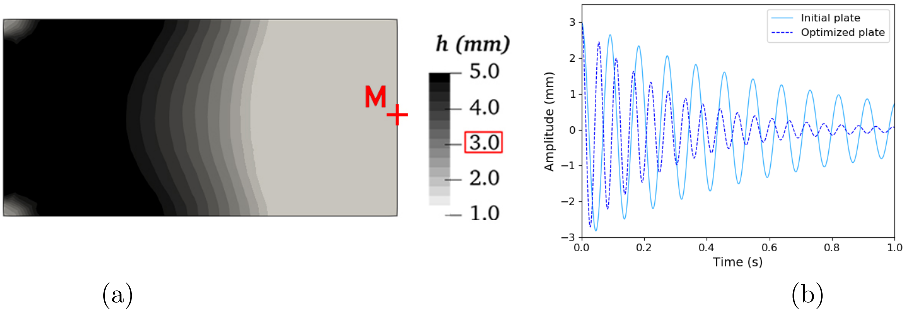

(a) (b)

FIGURE 8. (a) Thickness profile of the optimized plate and (b) free vibration amplitudes of the initial and optimized plates at M for the generalized Maxwell material.

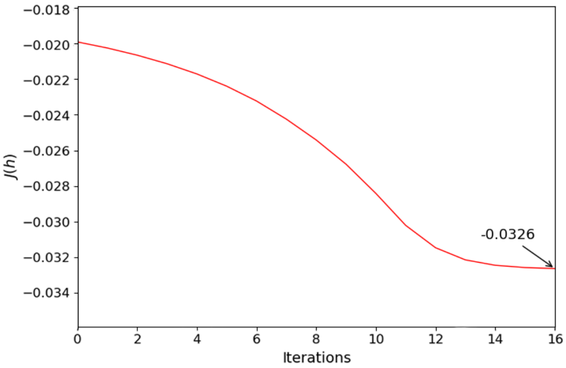

FIGURE 9. Cost function convergence with respect to the number of iterations for the damping optimization of the generalized Maxwell rectangular plate.

the eigenmodes are mostly independent of the material properties and similar from one optimization to another. Therefore, they will not be further investigated. In the same way, the final designs of initially shorter and wider plates are similar and provide no additional information.

The Zener model is now used to explore the impact of the material parameters. The reference values are still: $E_\infty = 18$ MPa, $E_1 = 30$ MPa, $\tau_1 = 0.001$ s, added of Poisson's ratio values $\nu_\infty = 0.499$ and $\nu_1 = 0.498$ corresponding to $K = 3$ GPa. The modulus E_1 has a considerable impact on the final design of the plate represented Figure 10. If the value of E_1 decreases while the other parameters are kept constant, the free vibration becomes less dampened and the material is increasingly accumulated to the clamped end of the plate.

The relaxation time is also an impactful parameter, Figure 11 shows the final designs for 3 different values of τ_1. For high values of relaxation time the material is accumulated at the free extremity of the plate decreasing its frequency and decay rate. For extreme values of τ_1, the behavior tends to be purely elastic, therefore the corresponding vibration curves for the initial plates are less dampened than the curve corresponding to an intermediate value. However, the free vibration amplitudes of the optimized plate for high values of relaxation time are completely different due to its pendulum-like design.

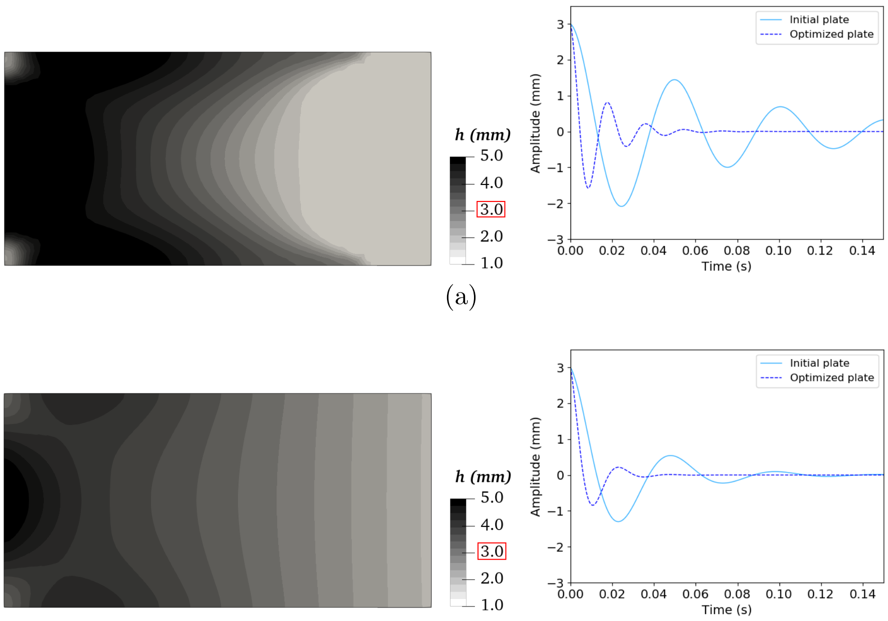

(a)

(b)

Figure 10. Thickness profiles and free vibration amplitude for (a) the reference Zener material and (b) the same material parameters except for $E_1 = 40$ MPa.

3.4.2. *Shape optimization.* The shape optimization of the generalized Maxwell material is now performed while maintaining the thickness constant. Similarly to the previous cases, the material is redistributed toward the clamped end of the plate increasing the frequency and the decay rate of the free vibrating structure (Figure 12). The shape of the plate significantly changes in order to achieve optimal performance. Additionally, the final value of the cost function in this example is close to the final value of the sizing optimization, the comparison of the convergence curves Figure 9 and 13 shows a similar gain for the selected sets of admissible design parameters.

3.4.3. *Coupled optimization.* Both the thickness and the shape are now optimized alternatively. For the generalized Maxwell viscoelastic material, the final design is represented Figure 14. The coupled optimization provides a substantial gain in damping capacity as shown by the vibration curves. The final value of the cost function is also significantly lower due to the combined optimization of the two previous design parameters (Figure 15).

The Zener model is now used for material parameter analysis. As for the sizing optimization, the modulus of the viscoelastic branch E_1 has a considerable impact on the thickness profile but also on the shape of the plate (Figure 16).

The last parameter of interest is Poisson's ratio. In a first example, ν_0 is fixed and the impact of ν_1 on the optimized results is studied. As one read in Figure 17, this parameter also has a strong impact on the shape of the optimized plate. Although, their Poisson's ratios differ for only 0.02, the designs displayed for cases *a*) and *b*) are noticeably different. However, the free vibration amplitudes show that the damping remains almost unchanged, only the final designs are different. We have obtained different designs that may drive to similar behavior in terms of free vibrations

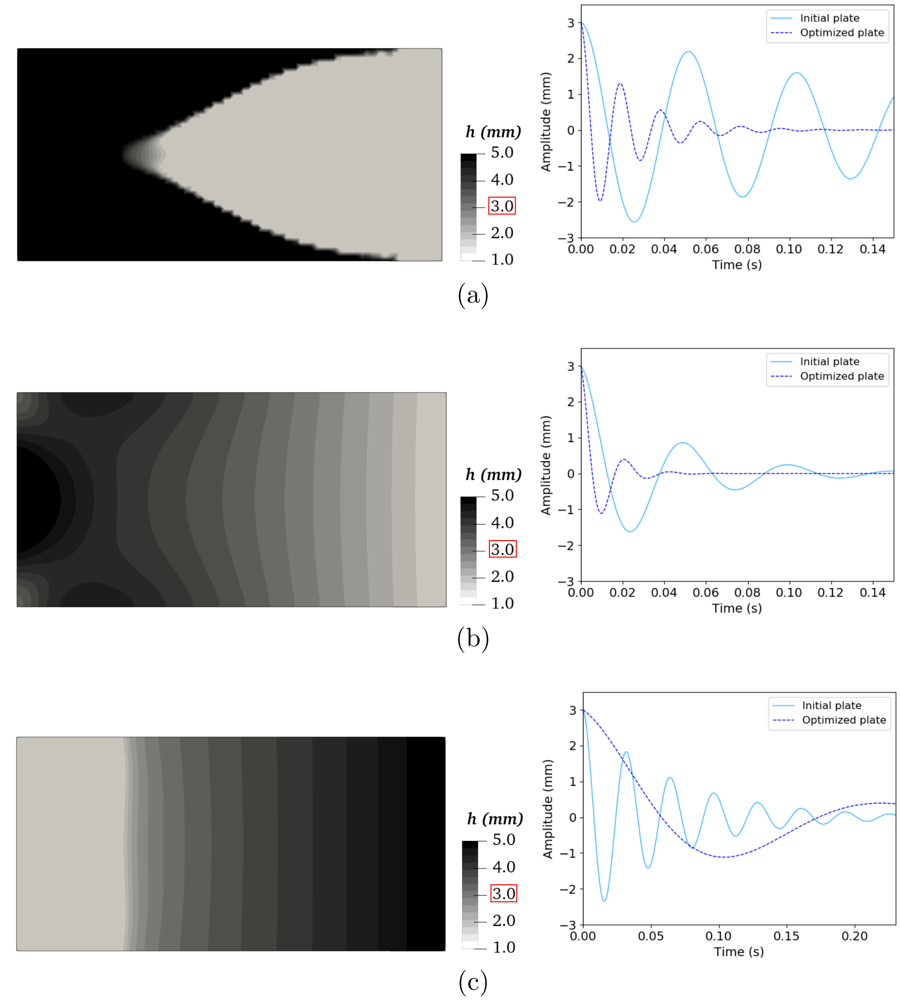

FIGURE 11. Thickness profiles and free vibration amplitudes of Zener optimized plates characterized by different relaxation times (a) $\tau_1 = 0.0005$ s (b) $\tau_1 = 0.002$ s (c) $\tau_1 = 0.02$ s.

which is interesting for accommodating engineering constraints. Assumptions of either constant Poisson's ratio or constant bulk modulus are considered. While the former is the most commonly used and has proved to be a way to simplify the numerical resolution, the latter may provide a more accurate representation of actual material behaviors.

Considering our generalized Maxwell material, Poisson's ratio is first assumed constant in every Maxwell branch. According to the couples (E_j, τ_j), two different configurations may be happening, the final design is either a sharp profile with saturated bounds (Figure 18), or a smooth profile (Figure 19). When sharp profiles are obtained, the same local minima are reached for a range of Poisson's ratio values, as illustrated by Figure 18, where two sharp configurations have been obtained for Poisson's ratio on either side of the threshold value 0.465.

When smooth profiles are obtained, Poisson's ratio impacts the final design, but without noticeably modifying the vibration damping. The magnitude of these

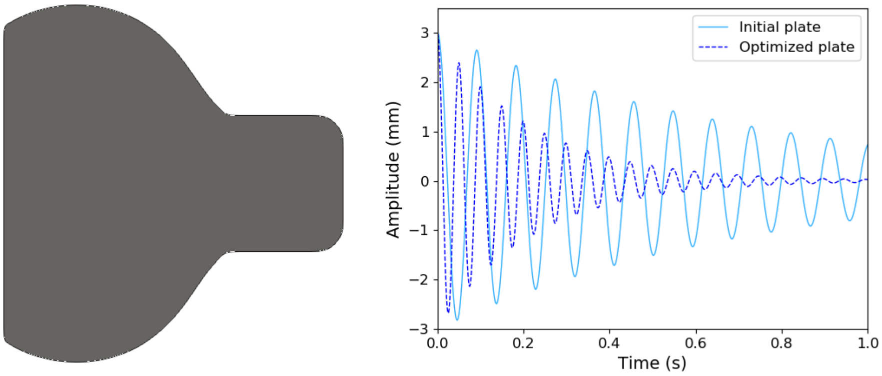

(a) (b)

FIGURE 12. (a) Optimized shape for a constant $3mm$ thick plate and (b) the resulting free vibration amplitudes of the optimized plate compared to the rectangular plate free vibration.

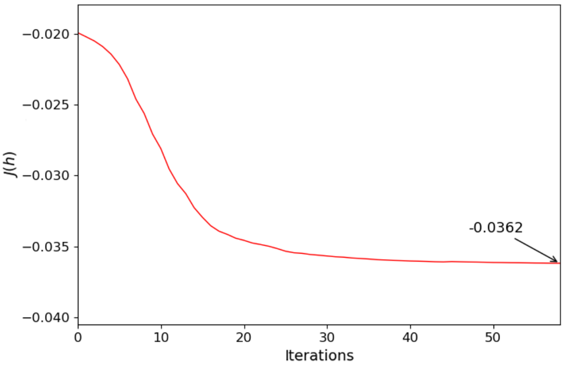

FIGURE 13. Cost function convergence with respect to the number of iterations of the shape optimization for the generalized Maxwell material.

variations depends on the material, they may be important as previously discussed or less significant (Figure 19).

Finally, the bulk modulus is assumed constant and the frequency dependence of Poisson's ratio is taken into account. Unlike when ν is considered constant, this assumption ensures that the optimization does not lead to the wrong local minimum when sharp profiles are obtained. For smooth profiles, the results accuracy is enhanced with increasing ranges of Poisson's ratio.

3.4.4. *A peek at the opposite problem: limiting the damping effect.* For other applications where high frequency and low decay rate are valued, one can be interested in the minimization of the logarithmic decrement. Running shoes, demanding efficient bouncing properties, are an example of such applications. Minimizing the logarithmic decrement of a viscoelastic cantilever plate leads to a structure where the material is allocated at the free end, saturating the optimization bounds and decreasing both the vibration frequency and decay rate. In the range of viscoelastic properties commonly shown by polymers, the material distribution of the optimized

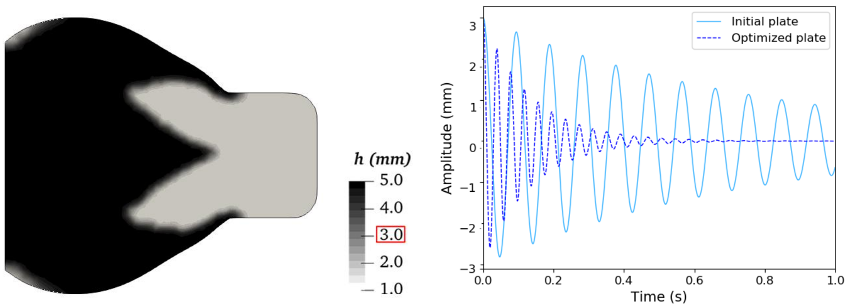

(a) (b)

FIGURE 14. (a) Optimized shape and thickness profile for $h_0 = 3mm$ initial plate thickness and (b) free vibration amplitudes of the optimized and initial plates.

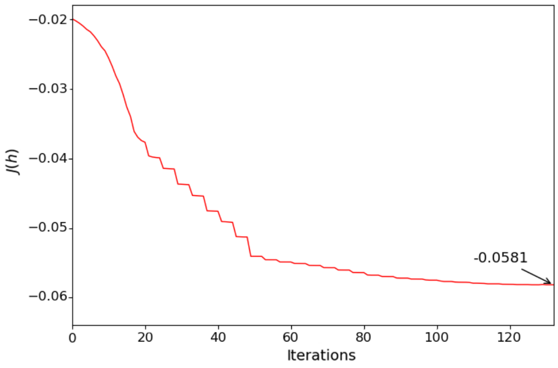

FIGURE 15. Cost function convergence with respect to the number of iterations for the coupled optimization of the generalized Maxwell rectangular plate.

plate does not depend on the material parameters and is always similar from one optimization to another. To satisfy industrial needs, a more flexible objective function may be used, such as

$$\mathcal{J}(h, \Omega) = \omega_i(h, \Omega) + k\frac{1}{\omega_r(h, \Omega)} \tag{33}$$

where k is a constant related to the frequency penalty. The penalty parameter allows to set priority between high vibration frequency and low decay rate depending on the application. Figure 20 shows the variation of decay rate with respect to the frequency for various values of k as well as the different final designs. For $k = 1$ the shape is identical to the previous case, the material is entirely allocated to the free end of the plate. As k increases, the material tends to be progressively redistributed to the clamped end.

4. CONCLUSION

Viscoelastic structures optimized by the proposed algorithm show a substantially improved damping capacity. The optimization results also show the high influence

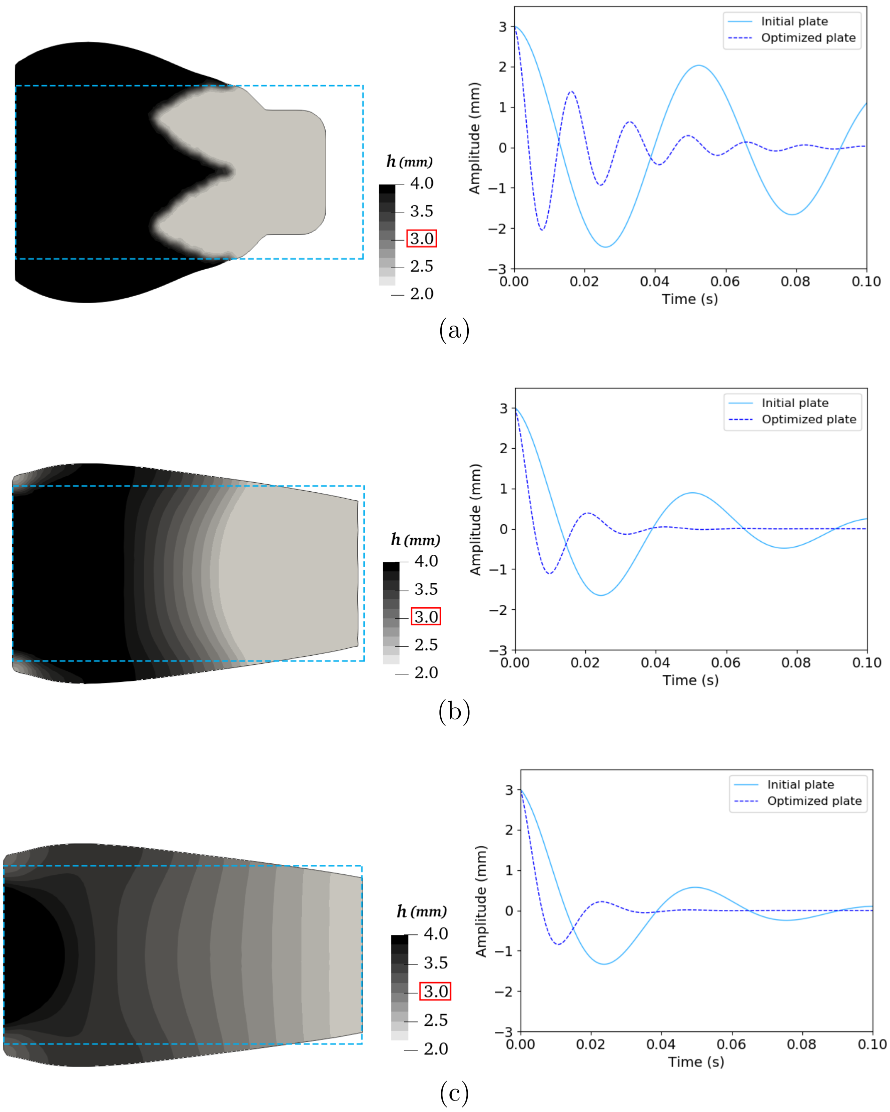

FIGURE 16. Thickness profiles and free vibration amplitudes of the initial and optimized plates for a Zener material and different modulus (a) $E_1 = 10$ MPa (b) $E_1 = 30$ MPa (c) $E_1 = 40$ MPa.

of some material properties on the final design and on the free vibration amplitudes of the optimized structures. The Generalized Maxwell model used in this work allows to take into account the frequency dependence of the material properties. Poisson's ratio in particular is usually assumed constant in most works but has proved to be an impactful parameter in some cases. Solving this optimization problem using polynomial eigensolvers provides a way to apply optimization algorithms to actual viscoelastic materials whose spectrum of parameters have been determined experimentally. Therefore, it allows the use of such algorithms for industrial applications using experimental data.

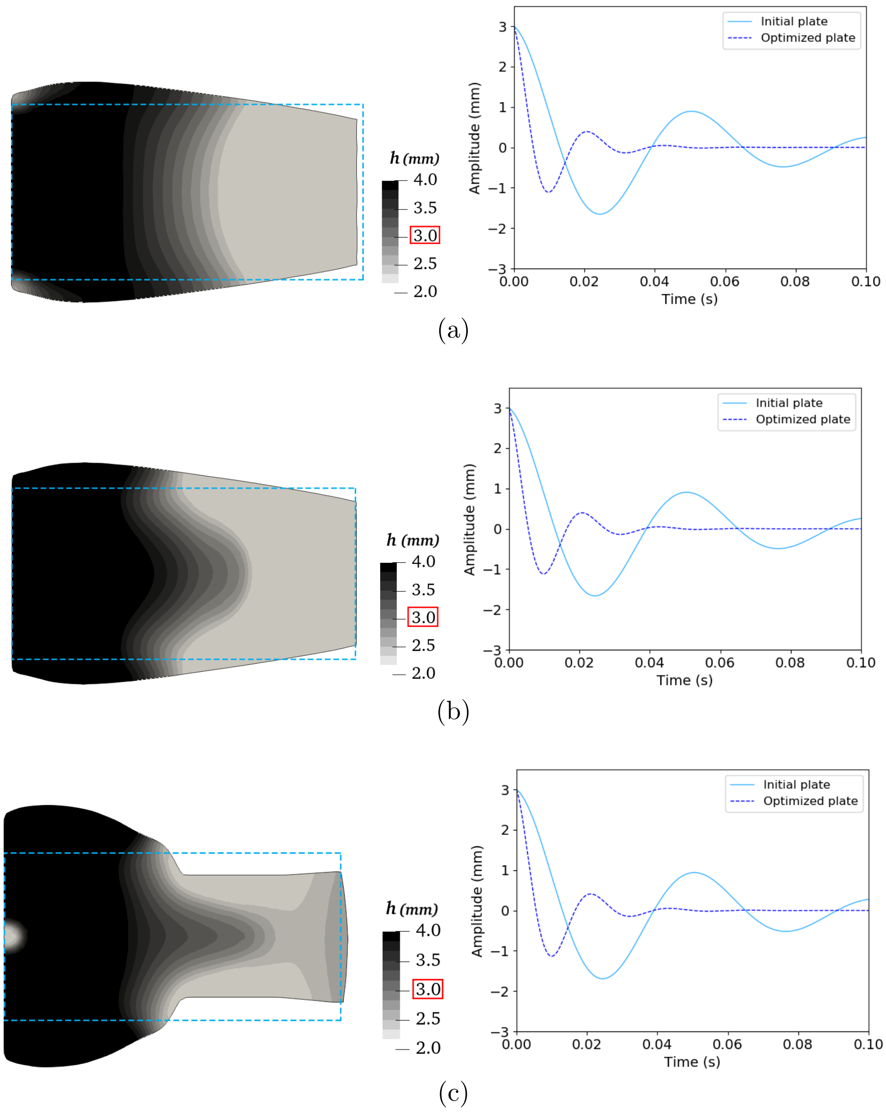

(a)

(b)

(c)

FIGURE 17. Thickness profiles and free vibration amplitudes of the considered plates for a Zener material and different Poisson's ratios (a) $\nu_1 = 0.498$ (b) $\nu_1 = 0.48$ (c) $\nu_1 = 0.4$.

ACKNOWLEDGEMENT

The work is part of the PhD of A.J. supported by the Chair "Modelling advanced polymers for innovative material solutions" led by Ecole polytechnique (l'X) and the Fondation de l'Ecole polytechnique and sponsored by Arkema. The authors would like to greatly acknowledge Pierre Jolivet for his advice and assistance with the interfacing of SLEPc and FreeFem++. The comments of the anonymous referees are gratefully acknowledged as they helped the authors to improve their final manuscript.

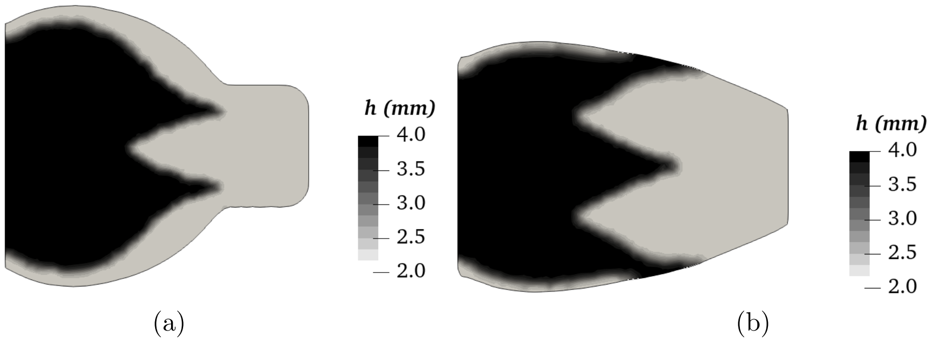

FIGURE 18. Examples of final designs of plates modeled by a Zener model for different ranges of Poisson's ratio values (a) $\nu \leq 0.465$ (b) $\nu > 0.465$.

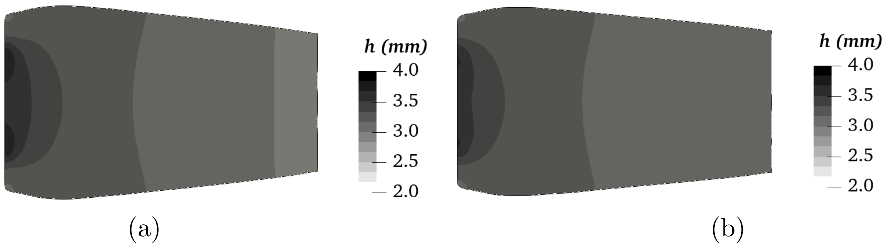

FIGURE 19. Possible designs of optimized plates for a Zener material and different Poisson's ratios (a) $\nu = 0.2$ (b) $\nu = 0.4$.

APPENDIX A. EXPRESSION OF THE BILINEAR FORMS

Let $(\omega, u) \in \mathbb{C} \times \mathcal{U}_2$ and $n \in \mathbb{N}_+^*$. The complex polynomial eigenproblem writes:

$$\sum_{j=0}^{n+2} \omega^j a_j(u, \hat{u}) = 0 \qquad \forall \hat{u} \in \mathcal{U}_2,$$

where the dependence on the thickness h has been dropped for the sake of readability. Denoting

$$\varphi(u, \hat{u}) = \frac{\partial^2 u}{\partial x^2}\frac{\partial^2 \hat{u}}{\partial x^2} + \frac{\partial^2 u}{\partial y^2}\frac{\partial^2 \hat{u}}{\partial y^2},$$

$$\psi(u, \hat{u}) = \frac{\partial^2 u}{\partial x^2}\frac{\partial^2 \hat{u}}{\partial y^2} + \frac{\partial^2 u}{\partial y^2}\frac{\partial^2 \hat{u}}{\partial x^2},$$

$$\xi(u, \hat{u}) = \frac{\partial^2 u}{\partial x \partial y}\frac{\partial^2 \hat{u}}{\partial x \partial y},$$

the bilinear forms are given by

$$a_0 = \int_\Omega -\frac{h^3}{12}\frac{E_0}{(1-\nu_0^2)}\left(\varphi(u, \hat{u}) + \nu_0 \psi(u, \hat{u}) + 2(1-\nu_0)\xi(u, \hat{u})\right) dA,$$

$$a_1(u, \hat{u}) = \int_\Omega -\frac{h^3}{12} p_1 \sum_{k=0}^{n} \frac{E_k}{1-\nu_k^2}\left(\varphi(u, \hat{u}) + \nu_k \psi(u, \hat{u}) + 2(1-\nu_k)\xi(u, \hat{u})\right) dA$$
$$+ \int_\Omega \frac{h^3}{12} \sum_{k=1}^{n} q_{1,k} \frac{E_k}{1-\nu_k^2}\left(\varphi(u, \hat{u}) + \nu_k \psi(u, \hat{u}) + 2(1-\nu_k)\xi(u, \hat{u})\right) dA,$$

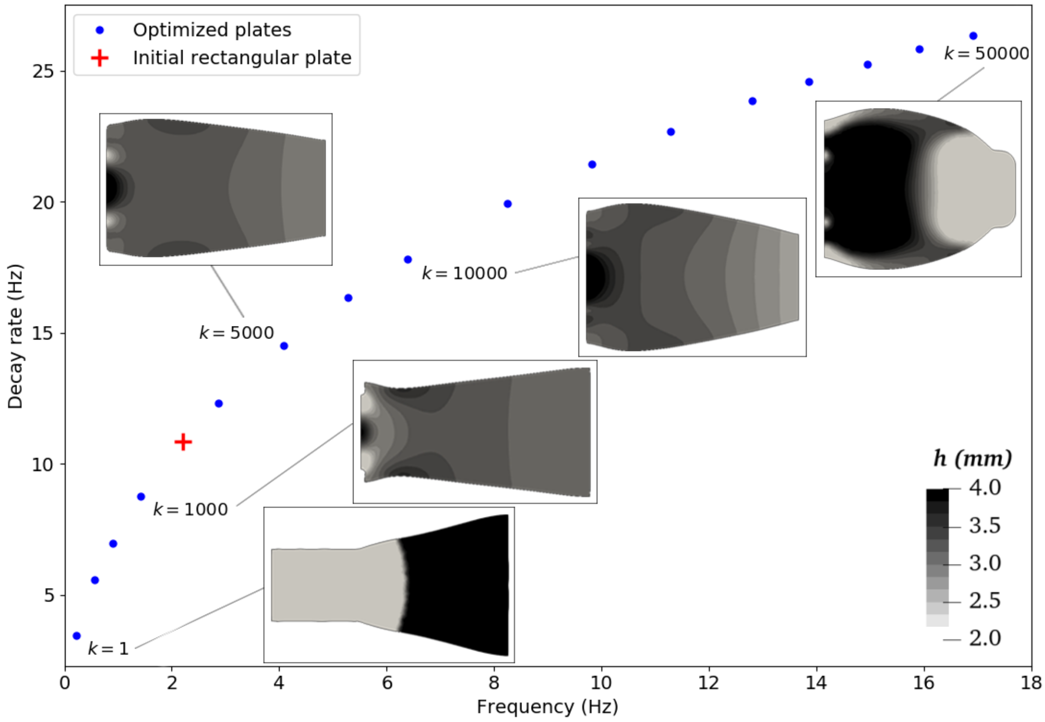

FIGURE 20. Decay rate with respect to the vibration frequency and design representations for plate inverse damping $\mathcal{J}(h,\Omega) = \omega_i(h,\Omega) + k\frac{1}{\omega_r(h,\Omega)}$ optimization.

$\forall j \in [\![2, n-1]\!]$,

$$a_j(u,\hat{u}) = \int_\Omega p_{j-2}\rho h u \hat{u}\, dA - \int_\Omega \frac{h^3}{12} p_j \sum_{k=0}^{n} \frac{E_k}{1-\nu_k^2} \left(\varphi(u,\hat{u}) + \nu_k \psi(u,\hat{u}) + 2(1-\nu_k)\xi(u,\hat{u})\right) dA$$

$$+ \int_\Omega \frac{h^3}{12} \sum_{k=1}^{n} q_{j,k} \frac{E_k}{1-\nu_k^2} \left(\varphi(u,\hat{u}) + \nu_k \psi(u,\hat{u}) + 2(1-\nu_k)\xi(u,\hat{u})\right) dA,$$

$$a_n(u,\hat{u}) = \int_\Omega p_{n-2}\rho h u \hat{u}\, dA - \int_\Omega \frac{h^3}{12} p_n \sum_{k=0}^{n} \frac{E_k}{1-\nu_k^2} \left(\varphi(u,\hat{u}) + \nu_k \psi(u,\hat{u}) + 2(1-\nu_k)\xi(u,\hat{u})\right) dA,$$

$$a_{n+1}(u,\hat{u}) = \int_\Omega p_{n-1}\rho h u \hat{u}\, dA,$$

$$a_{n+2} = \int_\Omega p_n \rho h u \hat{u}\, dA.$$

In the above the coefficients p_j and $q_{j,k}$ are defined through the expansions

$$\prod_{j=1}^{n}(1 + i\omega\tau_j) = \sum_{j=0}^{n} p_j \omega^j,$$

$$\prod_{\substack{j=1 \\ j\neq k}}^{n}(1 + i\omega\tau_j) = \sum_{j=0}^{n} q_{j,k} \omega^j.$$

References

[1] G. Allaire. *Conception optimale de structures*, volume 58 of *Mathématiques et Applications*. Springer, 2007.

[2] G. Allaire, C. Dapogny, and F. Jouve. *Shape and topology optimization, in Geometric partial differential equations, part II, A. Bonito and R. Nochetto eds.* Number 22 in Handbook of Numerical Analysis. Elsevier, 2021.

[3] G. Allaire and F. Jouve. A level-set method for vibration and multiple loads structural optimization. *Computer Methods in Applied Mechanics and Engineering*, 194:3269–3290, 2005.

[4] K. Ammari, A. Henrot, and M. Tucsnak. Asymptotic behaviour of the solutions and optimal location of the actuator for the pointwise stabilization of a string. *Asymptotic Analysis*, 28:215–240, 2001.

[5] E. Andreassen and J. Jensen. Topology optimization of periodic microstructures for enhanced dynamic properties of viscoelastic composite materials. *Structural and Multidisciplinary Optimization*, 49:695–705, 2013.

[6] M. Ansari, A. Khajepour, and E. Esmailzadeh. Application of level set method to optimal vibration control of plate structures. *Journal of Sound and Vibration*, 332(4):687–700, 2013.

[7] M. Bendsøe and O. Sigmund. *Topology optimization: theory, methods, and applications*. Springer Science & Business Media, 2013.

[8] J. Bicerano. *Prediction of Polymer Properties 3rd ed.*, volume 65 of *Plastics engineering*. New York : Marcel Dekker, 2002.

[9] J. Céa. Conception optimale ou identification de formes, calcul rapide de la dérivée directionnelle de la fonction coût. *Mathematical modelling and numerical analysis*, 20(3):539–552, 1986.

[10] D.-L. Chen, T.-C. Chiu, T.-C. Chen, M.-H. Chung, P.-F. Yang, and Y.-S. Lai. Using DMA to simultaneously acquire Young's relaxation modulus and time-dependent Poisson's ratio of a viscoelastic material. *Procedia Engineering*, 79:153–159, 2014.

[11] D.-L. Chen, T.-C. Chiu, T.-C. Chen, P.-F. Yang, and S.-R. Jian. Interconversions between linear viscoelastic functions with a time-dependent bulk modulus. *Mathematics and Mechanics of Solids*, 23:879–895, 2017.

[12] W. Chen and S. Liu. Microstructural topology optimization of viscoelastic materials for maximum modal loss factor of macrostructures. *Structural and Multidisciplinary Optimization*, 53:1–14, 2015.

[13] G. Delgado and M. Hamdaoui. Topology optimization of frequency dependent viscoelastic structures via a level-set method. *Applied Mathematics and Computation*, 347:522–541, 2019.

[14] J. Diani, P. Gilormini, and S. Arrieta. Direct experimental evidence of time-temperature superposition at finite strain for an amorphous polymer network. *Polymer*, 58:107–112, 2015.

[15] Z. Ding, J. Shi, Q. Gao, Q. Huang, and W.-H. Liao. Design sensitivity analysis for transient responses of viscoelastically damped systems using model order reduction techniques. *Structural and Multidisciplinary Optimization*, 64:1501–1526, 2021.

[16] A. Elsabbagh and A. Baz. Topology optimization of unconstrained damping treatments for plates. *Engineering Optimization*, 46:1153–1168, 2014.

[17] Z. Fang, L. Yao, S. Tian, and J. Hou. Microstructural topology optimization of constrained layer damping on plates for maximum modal loss factor of macrostructures. *Shock and Vibration*, 2020.

[18] Z. Fang and L. Zheng. Topology optimization for minimizing the resonant response of plates with constrained layer damping treatment. *Shock and Vibration*, 2015:11, 2015. Publisher: Hindawi.

[19] P. Freitas. Optimizing the rate of decay of solutions of the wave equation using genetic algorithms: A counterexample to the constant damping conjecture. *SIAM Journal on Control and Optimization*, 37:376–387, 1999.

[20] P. Geoffroy-Donders, G. Allaire, G. Michailidis, and O. Pantz. Coupled optimization of macroscopic structures and lattice infill. to appear in the International Journal for Numerical Methods in Engineering, 2020.

[21] M. Gröhlich, A. Lang, M. Böswald, and J. Meier. Viscoelastic damping design - thermal impact on a constrained layer damping treatment. *Materials and Design*, 207:109885, 2021.

[22] F. Hecht. New development in freefem++. *Journal of Numerical Mathematics*, 20:251–266, 2012.

[23] A. Henrot and M. Pierre. *Shape variation and optimization : a geometrical analysis*. Number 28 in Tracts in Mathematics. European Mathematical Society, 2018.

[24] V. Hernández, J. Román, and V. Vidal. SLEPc: A scalable and flexible toolkit for the solution of eigenvalue problems. *ACM Transactions on Mathematical Software*, 31:351–362, 2005.

[25] K. James and H. Waisman. Topology optimization of viscoelastic structures using a time-dependent adjoint method. *Computer Methods in Applied Mechanics and Engineering*, 285:166–187, 2015.

[26] K. James and H. Waisman. On the importance of viscoelastic response consideration in structural design optimization. *Optimization and Engineering*, 17:631–650, 2016.

[27] Z. Kang, X. Zhang, S. Jiang, and G. Cheng. On topology optimization of damping layer in shell structures under harmonic excitations. *Structural and Multidisciplinary Optimization*, 46:51–67, 2011.

[28] Q. Liu, D. Ruan, and X. Huang. Topology optimization of viscoelastic materials on damping and frequency of macrostructures. *Computer Methods in Applied Mechanics and Engineering*, 337:305–323, 2018.

[29] Z.-D. Ma, N. Kikuchi, and I. Hagiwara. Structural topology and shape optimization for a frequency response problem. *Computational mechanics*, 13(3):157–174, 1993.

[30] K. Rafetseder. *A new approach to mixed methods for Kirchhoff-Love plates and shells*. PhD thesis, Institute of Computational Mathematics, Altenbergerstraße 69 4040 Linz, Österreich, 2018.

[31] M. Rowbottom. The optimization of mechanical dampers to control self-excited galloping oscillations. *Journal of Sound and Vibration*, 75:559–576, 1981.

[32] J. Simon and F. Murat. Etudes de problèmes d'optimal design. volume 41, pages 54–62, Berlin, 1976. Springer Verlag.

[33] J. Soukup, F. Valeš, J. Volek, and J. Skočilas. Transient vibration of thin viscoelastic orthotropic plates. *Acta Mechanica Sinica/Lixue Xuebao*, 27:98–107, 2011.

[34] N. Tschoegl, W. Knauss, and I. Emri. Poisson's ratio in linear viscoelasticity - A critical review. *Mechanics of Time-Dependent Materials*, 6:3–51, 2002.

[35] I. Ward and J. Sweeney. *An introduction to the mechanical properties of solid polymers*. Wiley, 2 edition, 2004.

[36] K.-S. Yun and S.-K. Youn. Design sensitivity analysis for transient response of non-viscously damped dynamic systems. *Structural and Multidisciplinary Optimization*, 55(6):2197–2210, 2017.

[37] K.-S. Yun and S.-K. Youn. Topology optimization of viscoelastic damping layers for attenuating transient response of shell structures. *Finite Elements in Analysis and Design*, 141:154–165, 2018.

[38] G. Zhang and K. Khandelwal. Design of dissipative multimaterial viscoelastic-hyperelastic systems at finite strains via topology optimization. *International Journal for Numerical Methods in Engineering*, 119:1037–1068, 2019.